Available online at www.sciencedirect.com
SCIENCE DIRECT
Polymer 47 (2006) 2411–2422
polymer
www.elsevier.com/locate/polymer

Nanocomposites of poly(vinylidene fluoride) with organically modified silicate

Jennifer Buckley [a], Peggy Cebe [b,*], Daniel Cherdack [b], Jennifer Crawford [b], B. Seyhan Ince [b], Matthew Jenkins [c], Jingjing Pan [d], Matthew Reveley [b], Niesha Washington [e], Natalie Wolchover [b]

[a] *Department of Biology, Rochester Institute of Technology, Rochester, NY, USA*
[b] *Department of Physics and Astronomy, Tufts University, Medford, MA 02155, USA*
[c] *Department of Biotechnology, Rochester Institute of Technology, Rochester, NY, USA*
[d] *Department of Chemistry, Rochester Institute of Technology, Rochester, NY, USA*
[e] *Department of Biology, Gallaudet University, Washington, DC, USA*

Received 20 December 2005; received in revised form 3 February 2006; accepted 6 February 2006

Abstract

We report a study of the impact of cold crystallization on the structure of nanocomposites comprising poly(vinylidene fluoride) (PVDF) and Lucentite STN™ organically modified silicate (OMS). Nanocomposites were prepared from solution over a very wide composition range, from 0.01 to 20% OMS by weight. Thermal preparation involved cold crystallization at 145 °C of quenched, compression-molded plaques. Static and real-time wide and small angle X-ray scattering (WAXS, SAXS), Fourier transform infrared spectroscopy (FTIR), and differential scanning calorimetry (DSC) were used to investigate the crystalline phase of PVDF. For OMS content greater than 0.50 wt%, WAXS studies show that that the silicate gallery spacing increases modestly in the nanocomposites compared to neat OMS film, indicating a level of polymer intercalation.

Using Gaussian peak fitting of WAXS profiles, we determine that the composition range can be divided into three parts. First, for OMS greater than 0.5 wt%, alpha phase fraction, ϕ_{alpha}, is insignificant ($\phi_{alpha} \sim 0$–0.01). Second, at the intermediate range, for OMS between 0.5 wt% down to 0.025 wt%, beta phase dominates and the beta fraction, ϕ_{beta}, is related to alpha by $\phi_{beta} > \phi_{alpha}$. Third, below 0.025 wt% OMS, alpha dominates and $\phi_{alpha} > \phi_{beta}$. The ability of small amounts of OMS (≥ 0.025 wt%) to cause beta crystal domination is remarkable. Overall, crystallinity index (from the ratio of WAXS crystal peak area to total area) ranges from about 0.36 to 0.51 after cold crystallization. Real-time WAXS studies during heating of initially cold crystallized nanocomposites show that there is no inter-conversion between the alpha and beta phase PVDF crystals, where these crystals coexist at room temperature. While all samples showed a strong SAXS Bragg peak, indicating existence of two-phase lamellar stacks, the sample containing predominantly beta phase had poorly correlated lamellar stacks, compared to samples containing predominantly alpha phase.

Keywords: Nanocomposites; Organically modified silicates; Poly(vinylidene fluoride)

1. Introduction

Poly(vinylidene fluoride) (PVDF) is a technologically important semicrystalline polymer that is used as piezoelectric transducer film [1]. The PVDF molecule is highly polar (molecular dipole moment is $\mu_m \sim 7 \times 10^{-30}$ Cm) [2], and in three of the five crystallographic forms, the molecular dipoles are parallel, giving polar crystals and electrically active materials. The crystal forms of interest to the present work are the polar all-trans beta phase (also called form I), the non-polar TGTG′ alpha phase (form II) [3], and the polar TTTGTTTG′ gamma phase (form III) [4]. The orthorhombic alpha phase [5] is the form usually obtained during crystallization of PVDF from the melt, and special processing methods are required to obtain the pseudo-hexagonal polar beta phase [6] (for a review of PVDF crystal phases, see [2]). Typical methods to produce beta-PVDF use uniaxial or biaxial orientation with simultaneous application of an electric field (termed 'poling') to align the large spontaneous polarization of the beta crystals [7,8]. PVDF then exhibits the piezoelectric properties for which this polymer is best known [1].

* Corresponding author.
E-mail address: peggy.cebe@tufts.edu (P. Cebe).

0032-3861/$ - see front matter © 2006 Elsevier Ltd. All rights reserved.
doi:10.1016/j.polymer.2006.02.012

PVDF presents more than usual complexity because of the polymorphic transitions among the crystal phases [2,9,10]. At low crystallization temperatures, below about 150 °C, α-phase dominates [11]. At higher melt crystallization temperature [2] polymorphism occurs: the γ-phase nucleates early, but has a slower growth rate than α-phase so α-phase eventually dominates. Prest and Luca [9] showed that α could transform thermally to γ, and the transformation was enhanced by a surfactant. Later work [10] showed that a solid-state transformation from α to γ could occur, and γ also could be obtained by slowly melting samples that originally contained β-phase.

The impact of organo-clay nano-particle fillers on the crystal structure and polymorphism of the matrix polymer has been observed in nanocomposites of syndiotactic polystyrene, sPS [12], PVDF co-polymers [13], nylon 6 [14–21], and PVDF [22–27]. In the last two systems, one crystallographic phase forms in neat (unfilled) polymer, while another phase is favored in the nanocomposites.

In sPS [12], addition of clay decreased the crystallization half-time, serving as an efficient nucleating agent, and facilitating the formation of thermodynamically favored β-crystals. In the PVDF co-polymer with hexafluoropropylene [13], very large fractions of silica (up to ~35 wt%) caused reduction of crystallinity, and the authors suggest from thermal work that polymorphism of γ- and α-crystals of PVDF may occur. Using FTIR they found α-crystals coexisting with β- and γ-crystals. The proportion of β-crystals increased with silica content.

The nylon 6 and 6,6 systems have been extensively studied and shown to undergo crystal phase transitions from a high temperature α′ phase, to monoclinic α with H-bonds between anti-parallel chains, and thence by special treatments, to monoclinic γ, with H-bonds between parallel chains [28]. Upon heating the α-phase, a Brill transition is seen [29]. In nylon 6 nanocomposites, this complex polymorphism has been investigated using X-rays and DSC [14,15,17–20,30], FTIR [21], NMR [31], and dielectric relaxation [32].

Mathias and co-workers investigated nylon 6 nanocomposite system using ^{15}N nuclear magnetic resonance. They found that α (normally favored) co-exists with γ in nanocomposites and concluded that the clay 'stabilizes or/and induces the γ-phase of nylon 6' [31]. Interaction with the high surface area clay altered the macroscopic crystal properties. Fornes and Paul [18] suggest that crystallization of the γ form of nylon 6 is favored by conditions where polymer mobility is restricted. Lincoln, et al. [16] showed that crystallization is faster in nylon 6/OMS, and γ-phase is located preferentially near the surfaces of the silicate layers, while α-phase exists farther away [14]. In injection-molded parts, Fornes and Paul [18] showed that the skin was primarily γ-phase, while the core was mixed α- and γ-phase.

Nanocomposites of PVDF with Cloisite 6A organically modified silicate (OMS) were shown to crystallize into the beta phase, based on wide-angle X-ray scattering, WAXS [22]. Priya and Jog first reported the stabilization of the beta crystalline phase of PVDF in its nanocomposites with OMS [23,24]. These researchers used melt compounding to create their nanocomposites, and thermal annealing to show that the beta phase was stable. Work by our group [27] and others [25,26] investigated the tensile properties and structure of other PVDF/OMS nanocomposites in which beta phase crystals were obtained. Nanocomposites of PVDF with Nanomer OMS were recently prepared by extrusion compounding from the melt [33]. These authors studied compositions 0, 1, 2, and 5% OMS by weight and found the nanocomposites contained both alpha and beta crystals when processed from the melt. However, these works on PVDF nanocomposites [22,33] did not quantify the amounts of the two phases.

The present work reports a study of cold-crystallized PVDF nanocomposites made with Lucentite OMS over a very wide composition range, from 0.01 to 20.0 wt% OMS. The purpose of the study is to determine at what composition of OMS alpha and beta phase crystals co-exist. The quantity of the alpha and beta crystals is assessed using Gaussian peak deconvolution of the WAXS diffractograms. From this we determine that the composition range can be divided into three parts. First, for OMS greater than 0.5 wt%, alpha phase fraction, ϕ_{alpha}, is insignificant ($\phi_{alpha} \sim 0$–0.01). Second, at the intermediate range, for OMS between 0.5 wt% down to 0.025 wt%, beta phase dominates and the beta fraction, ϕ_{beta}, is related to alpha by $\phi_{beta} > \phi_{alpha}$. Third, below 0.025 wt% OMS, alpha dominates and $\phi_{alpha} > \phi_{beta}$. Real-time X-ray scattering studies show that the alpha and beta phase crystals melt separately, with no indication of inter-conversion between the phases. From analysis of the one-dimensional electron density correlation function on selected samples, we observe that the sample containing predominantly beta phase has lamellar stacks that are not as well correlated.

2. Experimental section

2.1. Sample preparation

The PVDF used in the present study was a Kynar based resin, obtained from Elf Autochem as grade 740, in pellet form. Lucentite STN™, was obtained from Zen-Noh Unico, America as fine powder. Lucentite is an organically modified layered silicate prepared by the supplier by ion-exchanging the Na ions in a synthetic smectite clay (Lucentite SWN, with a cation exchange capacity of approximately 0.65 mequiv/g) for tri octyl methyl ammonium cations [34].

PVDF was dissolved, and OMS was separately dispersed, in dimethylacetamide (DMAc) at room temperature with stirring for about 1–2 days. Both PVDF and Lucentite OMS formed transparent clear solutions in DMAc. Lucentite in DMAc was poured into a Petri dish and allowed to dry. A brittle Lucentite film was recovered and used for X-ray diffraction. For nanocomposites, OMS solution was added to the PVDF solution to achieve the desired weight ratio of OMS to PVDF, ranging from 0.01 up to 20.0% OMS by weight. The mixtures stirred at room temperature for several hours and were ultra-sonicated for 10 min before being poured into uncovered glass Petri dishes. Gentle heating at 40–70 °C for one day assisted in removal of DMAc. A thin, tough film resulted, that

could be easily lifted from the dish. Further drying of the film took place in a vacuum oven at room temperature for 1–2 weeks. Films were compression molded and quenched into cold water, then isothermally cold crystallized in an oil bath for 1 h after heating from room temperature to 145 °C. Samples of high OMS content, above 8.0 wt% OMS, were visually inhomogeneous, suggesting that these samples contained some poorly dispersed, large-scale OMS aggregates. As a result, most of our analyses were concentrated on the lower composition nanocomposites.

The nanocomposite samples will be referred to using a shorthand notation. L1.0 refers to the nanocomposite with 1.0% OMS; L0.025 refers to the nanocomposite with 0.025% OMS, etc. Homopolymer PVDF is designated as P100, and Lucentite OMS as L100.

2.2. Analysis methods

Room temperature WAXS studies were performed using a conventional sealed tube X-ray source having $\lambda = 0.1544$ nm. A Phillips PW1830 X-ray generator, operated at 40 kV and 45 mA, and optically encoded diffractometer, were used to investigate the range of scattering angles from $2\theta = 2$ to 30° (for θ the half-scattering angle). Films were examined in $\theta/2\theta$ reflection mode, using a step scan interval of 0.015° with 2.4 s/step; d-spacings were calibrated using silicon. The PVDF crystal peaks and amorphous halo were modeled using Gaussian wavefunctions. The total crystallinity index, ϕ_c, was determined from the Lorentz corrected intensity (i.e. from $I(q)q^2$ vs. q, for q the scattering vector, and $q = 4\pi \sin\theta/\lambda$), using the ratio of the area of coherent scattering peaks to the total curve area [35]. The fractions of alpha and beta phases, ϕ_{alpha} and ϕ_{beta}, were determined from the areas under the corresponding WAXS reflections, so that $\phi_{alpha} + \phi_{beta} = \phi_c$.

High temperature real-time simultaneous WAXS and SAXS were preformed at the Brookhaven National Laboratory, National Synchrotron Light Source, at beamline X27C. The wavelength was 0.1370 nm, and d-spacing was calibrated using sodelite and silicon for WAXS and silver behenate for SAXS. The sample was encapsulated using high temperature Kapton™ tape, and heated inside a Mettler FP90 hot stage. Intensity was accumulated every 30 s as the sample was heated from 140 to 180 °C at a rate of 1 °C/min. The intensity was corrected for changes in the incident beam intensity, sample absorption, and Kapton™ background. The Bragg long period was determined from the peak position of the scattering maximum in the SAXS Lorentz-corrected intensity plot, $I(q)q^2$ vs. q. The scattering invariant, Q, was determined from the total integrated intensity after all corrections, I_{corr}, using [35]:

$$Q = \int I_{corr}(q) q^2 \mathrm{d}q \tag{1}$$

The one-dimensional electron density correlation function was obtained from [36]:

$$K(z) = \int I_{corr}(q) q^2 \cos(qz) \mathrm{d}q \tag{2}$$

where z is a dimension along the normal to the lamellar stacks. Parameters such as the long period, L^{max}, crystal thickness, l_C, and linear crystallinity of the stacks, χ_{CL}, were determined using the method of Strobl and Schneider [36]. These parameters will be described later on when Fig. 11 is discussed.

Infrared studies were performed using a Bruker Equinox 55 Fourier transform infrared spectrometer equipped with an attenuated total reflectance cell. The resolution was 4 cm^{-1} and 32 scans were co-added to improve the signal to noise.

Differential scanning calorimetry (DSC) was performed on a TA Instruments 2920 Modulated DSC at a heating rate of 10 °C/min or 1 °C/min. Heat flow and temperature were calibrated using indium. Endotherms are presented with downward deflection. The degree of crystallinity of PVDF was determined from the endotherm area using 104.6 J/g as the heat of fusion of 100% crystalline PVDF [37].

3. Results and discussion

3.1. Static wide angle X-ray scattering studies

The WAXS scattering from Lucentite OMS is shown in Fig. 1. Five orders of the silicate gallery spacing can be seen, and these are plotted in the inset according to Bragg's law, $n\lambda = 2d_{100}\sin\theta$. The inset plots n vs. 2 sin θ/λ, from which the spacing d_{100} is determined to be 1.75 nm. This is smaller than the d-spacing we reported on Lucentite powder samples [38]. Lucentite OMS untreated powder samples showed two orders of the silicate gallery spacing peak, d_{100}(OMS) = 1.90 nm, and d_{200}(OMS) = 0.92 nm. The shorter d-spacing and higher degree of order seen in the L100 film is possibly a result of the treatment in DMAc solvent.

Fig. 2(a) and (b) shows WAXS intensity vs. 2θ, for representative high and low OMS compositions, respectively. Fig. 2(a) shows the gallery spacing of Lucentite OMS at low angle. Note that several samples, including L8 and L1.5 in Fig. 2(a) show several higher orders of the Lucentite OMS d_{100} peak. In samples of low OMS content (OMS < 0.1 wt%),

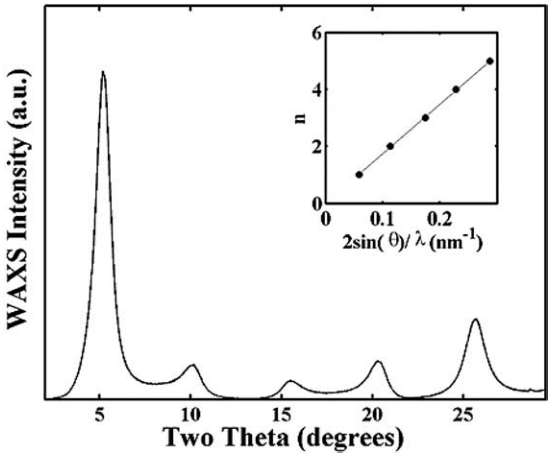

Fig. 1. WAXS intensity vs. scattering angle, 2θ, for Lucentite OMS, L100, showing five orders of the gallery spacing reflection. The inset shows index, n, from Bragg's law, vs. 2 sin θ/θ. Lucentite d_{100} is determined from the slope.

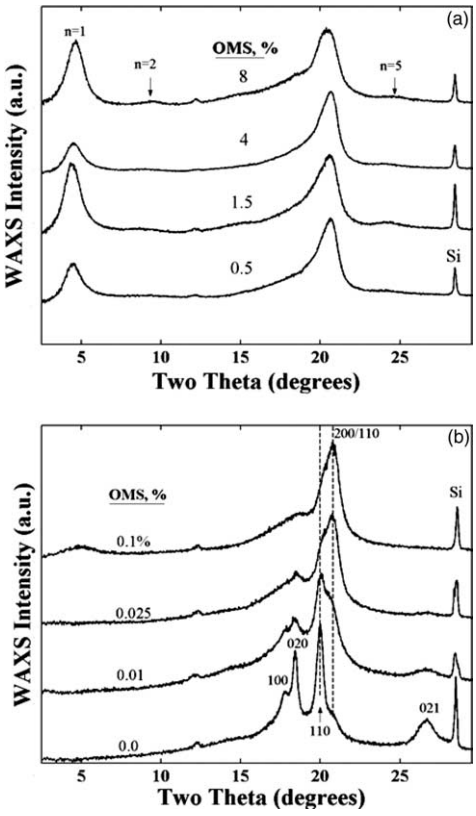

Fig. 2. WAXS intensity vs. scattering angle, 2θ, for nanocomposites of PVDF with Lucentite OMS. Wt% OMS is listed on the graph. (a) High OMS content nanocomposites, L0.5, L1.5, L4 and L8, showing the Lucentite OMS d_{100} gallery spacing peak below $2\theta \sim 4°$ and two higher orders marked $n=2$ and 5. (b) Low OMS content nanocomposites, L0.01, L0.025, and L0.10 and PVDF. No gallery spacing peak was seen in the samples with OMS content below 0.10 wt%. In part (b), the Miller indices for alpha PVDF are listed on the bottom curve, while the (200)/(110) beta PVDF reflection is marked on the uppermost curve. The silicon standard peak is marked Si.

no diffraction from the gallery spacing at low angle was seen. For L0.5, L1.5, L5, and L8 (Fig. 2(a)) a single major reflection is seen in the higher angular range from 16 to 22°, characteristic of beta PVDF. The peak at $2\theta = 20.78°$ corresponds to $d_{200/110}(\beta) = 0.427$ nm [6]. Gamma phase PVDF has a very similar d-spacing reflection at $d_{021}(\gamma) = 0.431$ nm [4], but no other reflections of the gamma phase were observed. In particular, we did not observe the gamma phase reflection from (111) planes, that occurs at $d_{111}(\gamma) = 0.39$ nm [4], and which does not overlap any of the alpha or beta phase reflections. The alpha phase of PVDF has four major reflections, marked on the lowest curve of Fig. 2(b). The dashed lines call attention to the diminution of the alpha phase (110) reflection and the simultaneous increase in the beta phase (200)/(110) reflection as the OMS content increases.

Using the positions of the higher order reflections, more accurate estimate of the gallery spacing in the nanocomposite can be made, as suggested by the inset in Fig. 1. These data are listed in Table 1 along with the d-spacings of the PVDF/OMS nanocomposites that showed gallery spacing reflections. All of the polymer nanocomposite samples showed d_{100}-spacing values greater than that of L100, ranging in the nanocomposites from 1.79 to 1.84 nm. This modest increase in the d_{100}-spacing suggests a low level of intercalation of the PVDF in the OMS galleries. We conclude that in nanocomposites with OMS content at or above 0.1 wt%, the OMS is not completely exfoliated; some level of PVDF intercalation occurs. We cannot rule out the possibility that there is also partial exfoliation of OMS in the samples with smaller OMS content.

Table 1
OMS gallery spacings in PVDF/OMS nanocomposites with high OMS content compared to Lucentite OMS

Sample[a]	d_{001} (nm) (± 0.05)
L0.1	1.77
L0.25	1.80
L0.5	1.82
L0.75	1.83
L1	1.82
L1.5	1.84
L4	1.82
L8	1.79
L16	1.84
L20	1.84
L100	1.75

[a] Samples are designated as Lxxx where xxx represents the wt% of OMS.

Since beta phase PVDF had been reported in nanocomposites with Cloisite 6A organically modified silicate [22–24], we were not surprised originally to observe strong beta phase signature in PVDF nanocomposites with Lucentite OMS in compositions from 2 to 20 wt%. We decided systematically to reduce the OMS content to find the range of compositions at which the crossover from beta-domination to alpha-domination occurred. Under the processing conditions used in this study (compression molding followed by cold water quench and cold crystallization at 145 °C), when the OMS composition is 0.025 wt% or greater, beta phase dominates the crystal structure.

Lower OMS content samples are shown in Fig. 2(b). For L0.10, a single major reflection is seen in the range from 18 to 22°. The peak at $2\theta = 20.78°$ corresponds to $d_{200/110}(\beta) = 0.427$ nm [6]. Gamma phase PVDF has a very similar d-spacing reflection at $d_{021}(\gamma) = 0.431$ nm [4], but no other reflections of the PVDF gamma phase were observed. As the OMS content decreases, reflections characteristic of alpha phase are also observed. In the P100 scan (bottom curve in Fig. 2(b)) the Miller indices of alpha phase reflections are marked at $2\theta = 17.8$, 18.5, 20.1, 26.7° for $d_{100}(\alpha) = 0.494$ nm, $d_{020}(\alpha) = 0.480$ nm, $d_{110}(\alpha) = 0.443$ nm, and $d_{021} = 0.334$ nm, respectively [5]. The two dashed lines in Fig. 2(b) mark the peak positions of the 200/110-beta reflection, and the strongest reflection from the alpha phase, 110-alpha. As OMS content increases above 0.025%, all alpha peaks diminish leaving only the broad beta peak.

To estimate the crystallinity index and fractions of alpha and beta phase PVDF in samples with lower OMS content, the WAXS peaks were fitted with Gaussian profiles using a Nelder–Mead simplex direct search routine [39]. The Lorentz-corrected scattered intensity, Iq^2 vs. q was fitted with a sum of

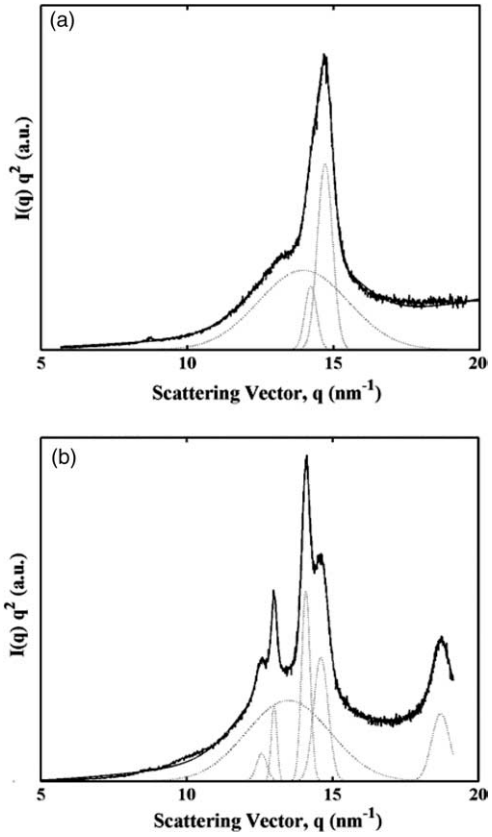

Fig. 3. Deconvolution of the Lorentz-corrected WAXS intensity, $I(q)q^2$ vs. q, using Gaussian wavefunctions, for PVDF/OMS nanocomposites with (a) high OMS content, exemplified by L0.10; (b) low OMS content, exemplified by L0.015. Heavy line—measured data; light line—summation of Gaussian peaks; dotted lines—individual Gaussian peaks.

Gaussians and a quadratic baseline:

$$I(q)q^2 = \sum \left\{ A_i \exp\left(\frac{(q - q_{0i})^2}{2\sigma_i^2} \right) \right\} + Bq + Cq^2 \tag{3}$$

where A_i is the amplitude, q_{0i} is the mean q-vector, σ_i is the standard deviation, and B and C are the q and q^2 coefficients of the quadratic, respectively. Examples of this procedure are shown in Fig. 3(a) and (b) for L0.10 (more beta than alpha phase) and L0.015 (more alpha than beta phase), respectively. The angular range of the silicon reference peak was eliminated from the fit. We were unable to fit the peaks in samples with larger content of OMS (OMS $\geq$ 1.0 wt%), because of uncertainty in the shape of the amorphous halo. Therefore, this approached was applied only to samples with OMS content less than 1.0 wt%. Total crystallinity index, ϕ_i, is listed in the second column of Table 2. Variations in the amorphous halo position and intensity contribute to the scatter seen in the crystallinity indices.

The alpha (or beta) fraction, ϕ_{alpha} (or ϕ_{beta}), was estimated from the ratio of the area of the alpha peak (or beta peak) to the total area. The dependence of total crystallinity index, beta fraction and alpha fraction on OMS concentration is shown in Fig. 4(a)–(c) in a plot whose x-axis is $\log_{10}$(OMS concentration). Solid symbols are used for nanocomposites; open symbols are used for homopolymer PVDF. To include the homopolymer PVDF on this logarithmic plot, for comparison purposes, solid symbols are placed at an arbitrary x-position on the left and shown with open symbols. Total crystallinity index is shown in Fig. 4(a) for nanocomposites (solid squares) and P100 (open square). Alpha and beta contents are shown in Fig. 4(b) (circles) and (c) (up triangles), respectively. Also included for comparison are high temperature data taken at

Table 2
Properties of PVDF/OMS nanocomposites: WAXS crystallinity index, melting temperature, heat of fusion, and mass fraction crystallinity

Sample[a]	ϕ_{ci}[b] (±0.03)	T_{m1}[c] (°C)	T_{m2}[c] (°C)	T_{m3}[c] (°C)	ΔH_f[c] (J/g)	χ_c[d] (±0.02)
P100	0.49, 0.51	144, 159	166.7	[e]	45.6	0.44
L0.01	0.36	158	166	[e]	44.7	0.43
L0.015	0.45	[e]	166.7	[e]	42.9	0.41
L0.025	0.36	155	164	171	43.1	0.41
L0.05	0.37	155	164	172.5	42.9	0.41
L0.1	0.37	157	164	172.5	44.6	0.43
L0.25	0.37	153	164	172	46.4	0.44
L0.5	0.45	149	165	174	43.9	0.42
L1.0	[f]	150	162	171	37.2	0.36
L1.5	[f]	151	163	172	42.3	0.40
L2	[f]	153	166	171	45.4	0.43
L4	[f]	155	165	173	45.8	0.44
L8	[f]	155	166	171	45.4	0.43
L16	[f]	153	168	171	47.7	0.46
L20	[f]	154	166	171	48.1	0.46

[a] P100—homopolymer PVDF; nanocomposites with Lucentite are designated as Lxxx where xxx represents the wt% of OMS.
[b] Mass fraction crystallinity index from WAXS ratio of crystal peak area to total peak area.
[c] Data taken during heating at 10 °C/min.
[d] Mass fraction crystallinity from total area of the DSC endotherms using 104.6 J/g as heat of fusion of 100% crystalline PVDF [37].
[e] No peak was seen in this sample.
[f] Data could not be determined.

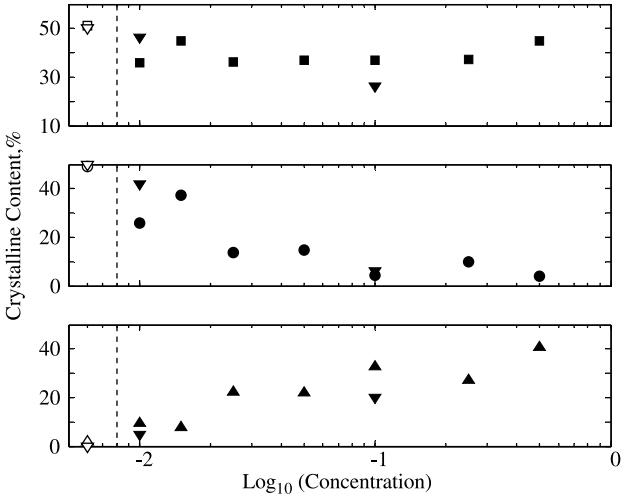

Fig. 4. Crystalline content, in percent, vs. $\log_{10}$(OMS concentration) determined from WAXS analysis. Data taken at an elevated temperature of 140 °C are shown with downward triangles in all parts of the figure. All other data were taken at room temperature. (a) Total crystalline content, ϕ_c; (b) alpha PVDF content, ϕ_{alpha}; (c) beta PVDF content, ϕ_{beta}. $\phi_{alpha}+\phi_{beta}=\phi_c$. The solid symbols refer to PVDF/OMS nanocomposites, for which the *x*-axis scaling applies. The empty symbols refer to homopolymer PVDF, with zero OMS content. The *x*-axis scale does not apply to these points, which are included for comparison only. The vertical line separates these points from the others.

140 °C during real-time X-ray studies (down triangles in all parts of the figure), which will be described later on.

Nanocomposite samples L0.010, L0.015, and L0.025 showed strong alpha phase peaks, viz. $d_{110}(\alpha)$ and $d_{020}(\alpha)$. As the concentration of Lucentite increased, the characteristic alpha peaks weakened, and the beta peak strengthened. However, in the range of OMS content from 0.10 up to 0.50 wt%, the alpha phase peak was small, but did not completely disappear. The WAXS scans could be fit with Gaussian profiles only when both beta and alpha characteristic peaks were included in the fit. In these nanocomposites, it appears that small amounts of the alpha phase coexist with beta, and the alpha d_{110} peak contributes to the asymmetry of the major WAXS peak on its low angle side.

We observe from Fig. 4(a) that homopolymer PVDF has total crystallinity index of about 0.50, and contains only alpha phase. Addition of only 0.025 wt% of Lucentite OMS causes the beta fraction to increase to ~0.20 and total crystallinity index to decrease to 0.36. A likely cause of the decrease of crystallinity, in this concentration range of OMS, is related to the competition between enhanced nucleation at lower OMS content, and reduction of chain mobility at higher OMS additions.

3.2. Analysis by infrared and thermal studies

The phase structure of PVDF has been identified using Fourier transform infrared spectroscopy [40–44]. Fig. 5(a) and (b) shows representative FTIR spectra for high and low OMS content samples, respectively. In Fig. 5(a), higher OMS content sample spectra show only the beta crystallographic

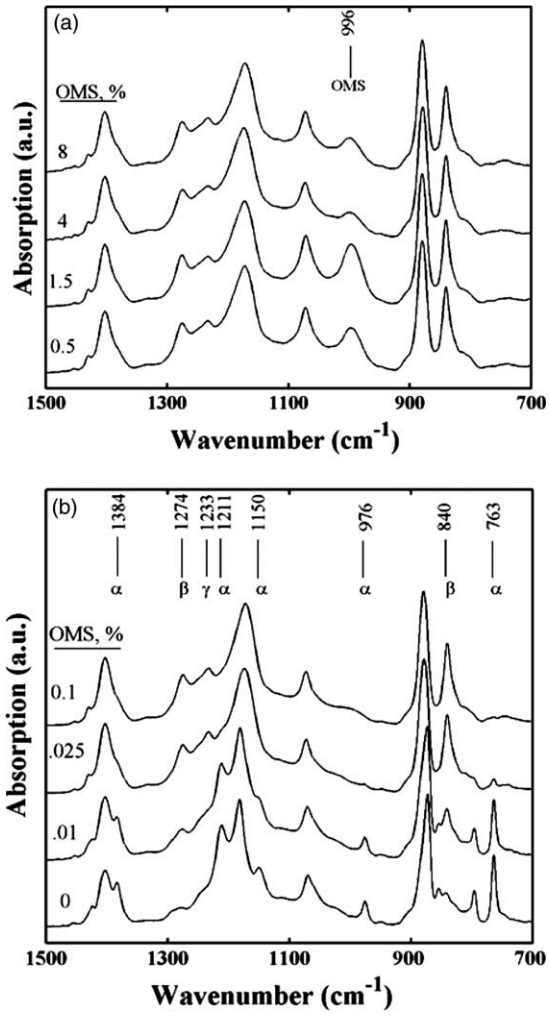

Fig. 5. Infrared absorbance vs. wavenumber for nanocomposites of PVDF with Lucentite OMS. (a) High OMS content nanocomposites, L0.5, L1.5, L4 and L8. (b) Low OMS content nanocomposites: L0.10 (top), L0.025, L0.01 and P100 (bottom). The positions of some representative bands are listed at the top, along with their phase identifications [40–42].

phase of PVDF, and two OMS bands. Absorption peaks at 1071 and 996 cm^{-1} are due to the Si–O stretching vibration, which has been reported for Montmorillonite clay [45]. The OMS band at 1071 cm^{-1} overlaps the 1071 cm^{-1} band of beta PVDF [40].

In Fig. 5(b), the lowest scan is P100, homopolymer PVDF, showing α-phase absorption bands [40] at 1384, 1211, 1150, 976, and 763 cm^{-1}. As the fraction of OMS increases from 0.01 wt% up to 0.10 wt% these bands decrease and the beta bands [40] at 1274 and 840 cm^{-1} increase. A tiny absorption band occurs at 1233 cm^{-1} that has been attributed to γ-phase PVDF [41,42]. PVDF β-phase does not normally form from the melt, though Lovinger [2] was able to trigger melt formation of beta epitaxially on KBr substrates. The fact that beta forms preferentially in PVDF/OMS nanocomposites, suggests that either the OMS nanoparticles are nucleating beta, perhaps epitaxially on their surfaces, or they may be interrupting the chain mobility during cold crystallization, so that the more extended-chain beta crystals are formed.

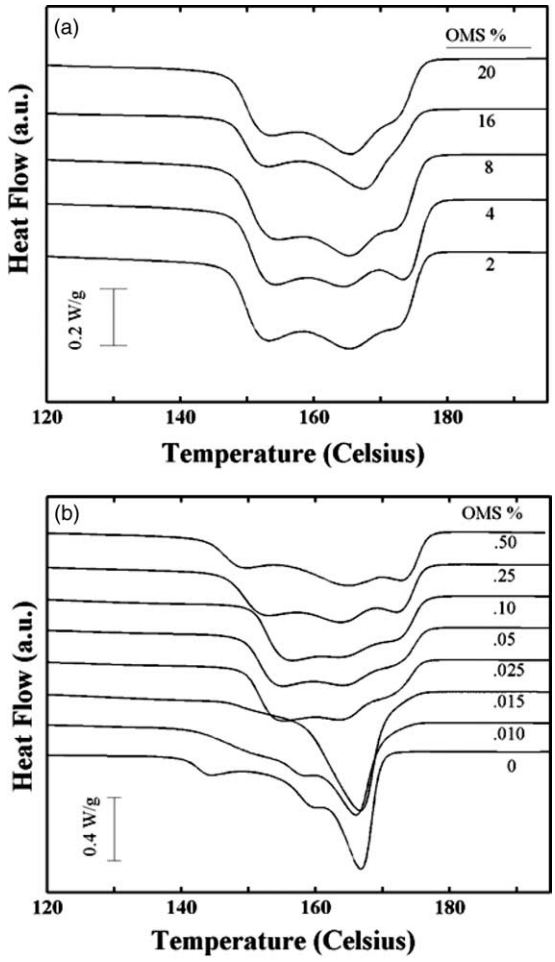

Fig. 6. Normalized heat flow vs. temperature of PVDF/OMS nanocomposites during heating at a rate of 10 °C/min. Wt% OMS is listed on the right. Endotherms are shown with downward deflection. Endotherms represent first heating of as-treated samples, quenched and then annealed at 145 °C. (a) High OMS content nanocomposites during heating. (b) Low OMS content nanocomposites during heating. The heat flow is shown normalized for total sample mass, but not for OMS content.

Thermal scans of the nanocomposites are shown in Fig. 6(a) and (b) for heating of high and low OMS content samples, respectively. Samples showing predominantly alpha phase PVDF (Fig. 6(b), including P100 homopolymer PVDF, L0.01 and L0.015) have a major melting endotherm at 166–167 °C. No higher melting endotherms, such as those that could be attributed to melting of PVDF gamma phase [11], are seen in these samples, but one or two weaker endotherms occur at lower temperatures. As the fraction of beta phase PVDF increases, a triplet of endotherms occurs with peak positions at approximately 153, 164 and 172 °C. Only samples containing beta PVDF showed the high temperature endotherm at 172 °C. The peak positions and areas of the endotherms and exotherms are listed in Table 2. The mass fraction degree of crystallinity was determined from the endotherm area and is included in the last column of Table 2.

PVDF has a low glass transition temperature of about −40 °C [46]. Because of the sub-ambient T_g, the nanocomposite samples were not quenched to a completely amorphous state, but crystallized to some extent during cooling. Subsequent thermal treatment at 145 °C anneals the least perfect crystals. The lowest endotherms in Fig. 6(a) and (b) result from the melting of the crystals annealed at 145 °C. The middle endotherm most likely results from melting of the primary crystal population formed during initial cooling. The upper melting endotherm results from the final melting of crystals that reorganized during the scan. For the three samples with lowest OMS content (P100, L0.01 and L0.015), the uppermost endotherm caused by reorganization and occurring at about 168 °C, is quite intense. Once the beta phase begins to dominate, for L0.025 the endotherm character changes. The uppermost endotherm relating to beta phase melting appears just above 170 °C, and the three endotherms have nearly the same intensity. Whereas some of these endotherms do overlap those seen in samples with alpha phase dominant, from X-ray analysis, no alpha reflections are seen once OMS content increases to 0.5 wt% and above. Therefore, all endotherms come from beta phase crystals formed either during initial cooling or annealing at 145 °C.

The impact of Lucentite OMS on the melting temperatures is shown in Fig. 7 for the thermal scans shown in Fig. 6. Homopolymer PVDF is included for comparison on the left side of the plot; the horizontal scale does not apply to these data. In samples with beta phase dominant, the upper endotherm above 170 °C (open circles) shows little dependence upon OMS. The middle endotherm for these samples (solid squares) is nearly flat at lower OMS content, and then trends upward a little. The independence of these two temperatures (of the middle and upper endotherm) to OMS content suggests that these endotherms arise from reorganized crystals.

On the other hand, the temperature of the lowest endotherm (open squares) first trends downward as OMS increases to

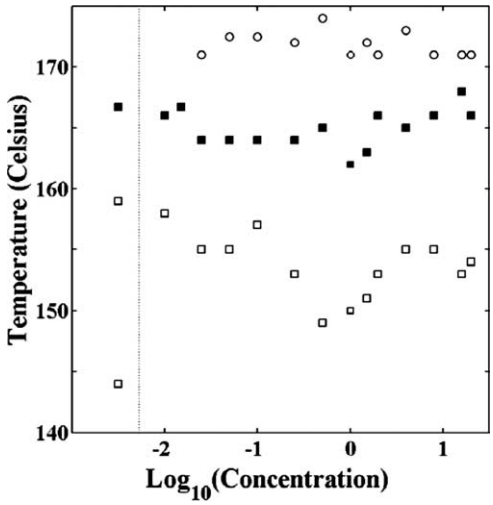

Fig. 7. Endotherm peak temperatures vs. $\log_{10}$(OMS concentration) of PVDF/OMS nanocomposites during DSC scanning at a rate of 10 °C/min. Endotherm temperatures represent first heating of as-treated samples, quenched then annealed at 145 °C; highest melting endotherm peak of beta PVDF—open circles; lower melting endotherms—squares. The symbols to the left of the dotted line refer to homopolymer PVDF, with zero OMS content. The *x*-axis scale does not apply to these points, which are included for comparison only.

0.5 wt%, and then increases again. Results from melt crystallization studies in our group [47] suggest that there is a competition between enhanced nucleation effect, at low OMS content, and inhibition of chain mobility, at higher OMS content. The composition that serves as the dividing point between these two effects is 0.5 wt%. Thus, the formation of the lowest endotherm, which is attributed to annealing of crystals formed during cooling, seems also to depend upon the prior crystallization and whether a nucleation enhancement or mobility impairment has occurred during cooling. This provides a possible explanation for the dependence of the lowest endotherm upon the OMS content. Dispersed layered silicates (modified and unmodified by surfactants) have been shown to act as nucleating agents to speed up the crystallization process in some polymers [48,49]. OMS has also been found to have mixed effect, which is the case here, in which the OMS acts as nucleation agent at lower OMS contents, but retards crystallization at higher concentrations [18,50]. The latter behavior is suggested to arise from reduced diffusion of chain segments to the growing crystal surface [45].

3.3. Real-time high temperature X-ray studies

Selected PVDF/OMS nanocomposite samples were investigated using high temperature real-time wide- and small angle X-ray scattering. WAXS results are shown in Fig. 8(a)–(c) for samples heated at 1 °C/min. Companion DSC scans at the same rate are shown in Fig. 9. The WAXS scans as a function of temperature are presented for P100, L0.01, and L0.10. These results show that the alpha and beta phase crystals melt

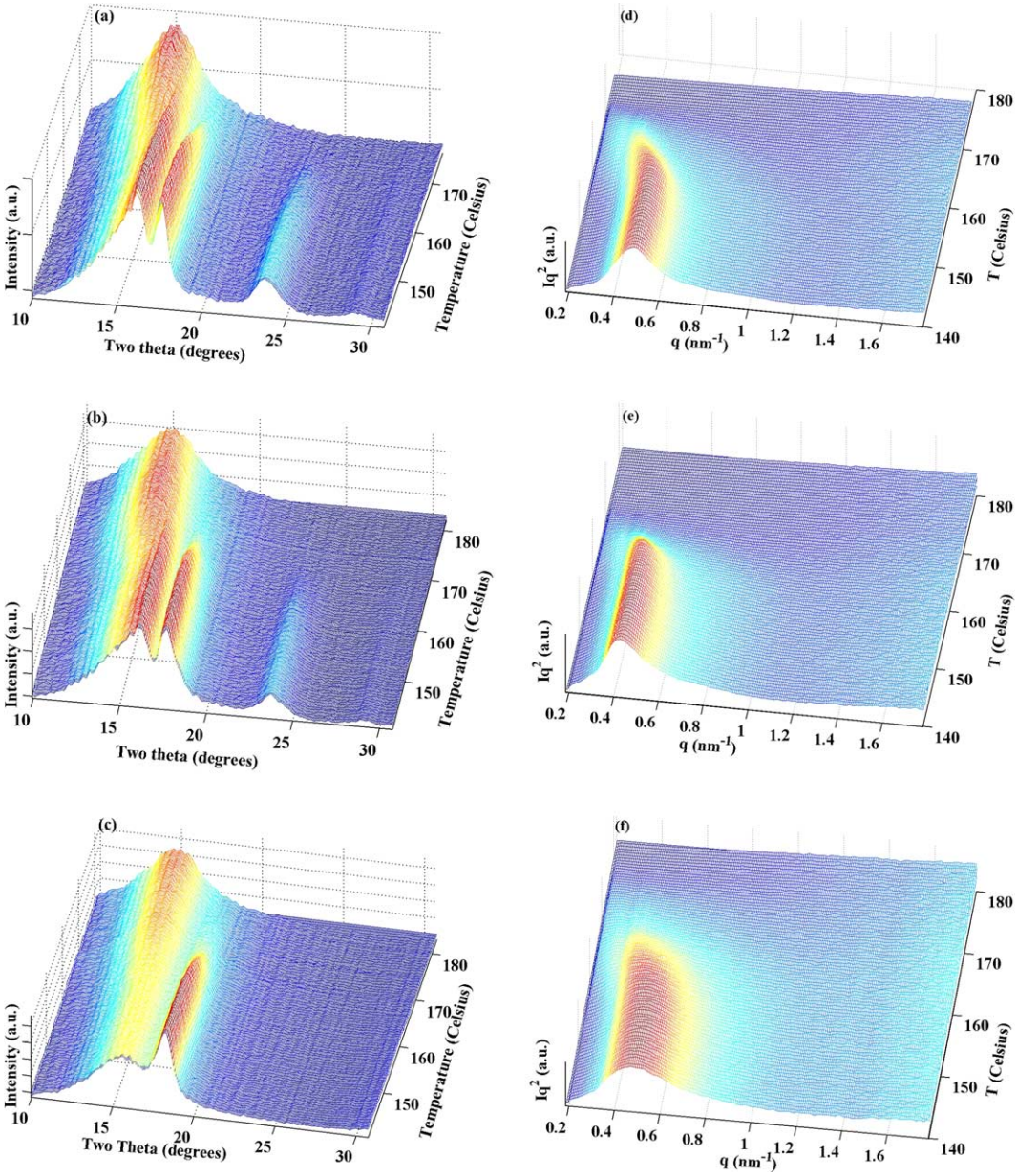

Fig. 8. Real-time WAXS intensity (a–c) or SAXS Lorentz–corrected intensity (d–f) during heating of PVDF/OMS nanocomposites at 1°C/min. (a),(d) P100 PVDF homopolymer; (b),(e) L0.01; (c),(f) L0.10.

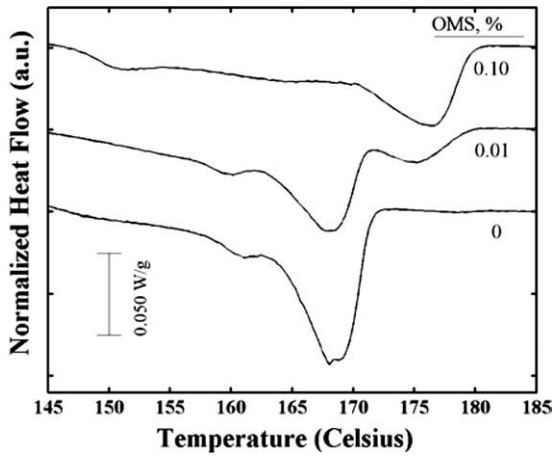

Fig. 9. Normalized heat flow vs. temperature of PVDF/OMS nanocomposites and PVDF during DSC scanning at a rate of 1.0 °C/min. Heat flow is shown normalized for sample mass, but not for OMS content.

separately, and no inter-conversion between the phases is seen during slow heating. The disappearance of the beta phase crystal reflection occurs over a slightly wider temperature range than for the alpha phase. Gaussian fitting was used to determine the initial crystallinity of these samples at the start of the scan at 140 °C. These data are included in Fig. 4(a)–(c) as the downward triangles. The high temperature crystallinity data confirm the overall trends (alpha phase decrease and beta phase increase) although the total crystallinity varied among the different samples.

Thermal scans are shown in Fig. 9 for the same set of samples. P100, bottom curve in Fig. 9, shows melting of alpha phase crystals peaking at about 169 °C. Sample L0.01 contains mixed alpha and beta crystals, with alpha dominant. A higher melting endotherm from beta crystals occurs at 177 °C, in addition to the melting endotherm of alpha crystals. All the peak melting temperatures are higher than in the samples heated at the faster rate (Fig. 7), which confirms the role of reorganization on the endotherm peak positions during slow heating.

The raw SAXS data of $I(q)q^2$ vs. q for the same three compositions are shown in Fig. 8(d)–(f). These data showed a single Bragg scattering peak, and were generally similar, except that the L0.10 nanocomposite sample with larger beta phase content, exhibited a broader SAXS peak than the other samples L0.01 and P100. The Bragg long period, L_B, and scattering invariant, Q, deduced from the Lorentz-corrected SAXS intensity data are displayed in Fig. 10(a)–(f). For all three nanocomposites, no Bragg peak could be determined for temperatures above about 168 °C, as the Bragg peak moves into the region of the beam stop. At the start of the heating, L_B is flat from 140 to 150 °C, and ranges from 13 to 15 nm. For P100 and L0.01, with alpha phase dominating, the steepest increase in L_B occurs between 160 and 168 °C, where the DSC (Fig. 9) shows the major melting peak. The scattering invariants also show steep decline in this temperature range. For P100, major melting is completed by about 172 °C, and the scattering invariant (Fig. 10(b)) reaches its minimum. L0.01 has a DSC melting peak from 170 to 180 °C, and this region corresponds to a gentle decrease in invariant.

L0.10, containing a large fraction of the beta phase, has its major melting peak (Fig. 9) from 170 to 180 °C, and shows no strong melting endotherm below this temperature (a weak endotherm appears at about 152 °C). The steady decrease of scattering invariant (Fig. 10(f)) from 160 to 180 °C suggests that the crystals in L0.10 are melting over a broad temperature range.

The scattering invariant is related to χ_{CL}, the linear crystallinity within the stacks, through [51]:

$$Q = \chi_L \chi_{CL}(1-\chi_{CL})(\rho_C^e - \rho_A^e)^2 \quad (4)$$

where χ_L is the fraction of material contributing to lamellar stack scattering, $(1-\chi_{CL})$ is the linear fraction of amorphous material within the stacks, and $\rho_C^e - \rho_A^e$ is the difference in electron density between the crystal and amorphous regions. According to Santa Cruz [51]:

$$\chi_L = \frac{\chi_C^{vol}}{\chi_{CL}} \quad (5)$$

where χ_C^{vol} is the volume fraction crystallinity determined from the DSC mass fraction crystallinity. If χ_L is equal to unity, all amorphous material resides within the lamellar stacks; if χ_L is less than unity, there will be amorphous regions located away from the lamellar stacks. The parameters χ_{CL} and χ_L are determined from analysis of the correlation function.

The one-dimensional electron density correlation function, $K(z)$, determined from Eq. (2) is plotted in Fig. 11(a) and (b). The upper part (a) of the figure shows the general correlation function, and the self-correlation triangle region formed by linearly extrapolating the low-z data to $z=0$ [36]. Also shown are the lamellar structural parameters, long period from first maximum past $z=0$, L^{max}; first minimum, $L^{min}/2$; and the shorter of the two correlation lengths in the two-phase structural model, l_1. The lower part (b) of the figure shows the actual data for P100 (solid circles), L0.01 (solid line) and L0.10 (dotted line). From the positions indicated in part (a), the values L^{max}, L^{min}, and l_1 are listed in Table 3 for the three samples.

In Fig. 11(b), following the method of Vonk [52]; $K(z)$ is normalized to a value of unity at $z=0$. The P100 PVDF homopolymer (solid circles) has a strong and sharp first maximum, and a strong second maximum. The lamellar stacks are well correlated to higher z-values. The nanocomposite L0.01 (solid line) also shows two strong maxima, and the position of the Bragg peak, L^{max}, is at higher z-value than in P100. The peak reflecting the stack periodicity is broader than in P100, and less intense, but the stacks are still well correlated to high z-value.

In comparison, L0.10 (dotted line) containing predominantly beta phase, has only one strong maximum beyond $z=0$, and the lamellar stacks lose their correlations at lower z-values than either of the other samples P100 or L0.01. This suggests that the larger amounts of OMS in L0.10, which induce

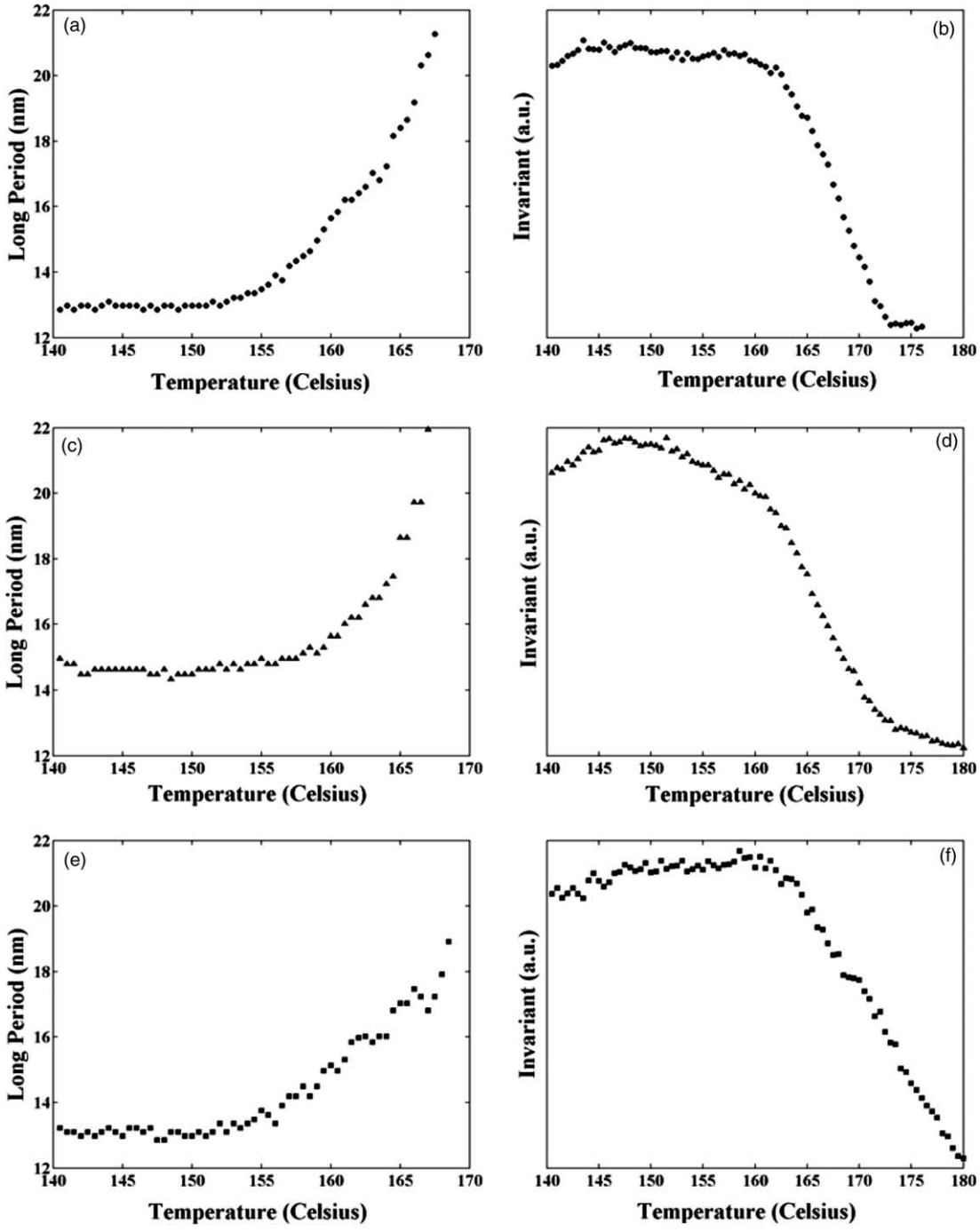

Fig. 10. Bragg long period, L_B, (a), (c), (e) and scattering invariant, Q (b), (d), (f), vs. temperature obtained during real-time SAXS studies of heating of PVDF/OMS nanocomposites at 1 °C/min. (a), (b) P100, PVDF homopolymer; (c), (d) L0.01; (e), (f) L0.10.

formation primarily of beta crystals, have lamellar stacks that are not as regular and comprise fewer lamellae per stack. While the stack periodicity L^{max} is about the same in L0.10 as in P100, the correlation of the stacks in L0.10 does not persist beyond the first maximum.

From Table 3 we see that the long period from correlation function first maximum past $z=0$, L^{max}, is greater than the value determined from the first minimum, L^{min}. According to Santa Cruz [51], if the lamellar stacks formed an ideal lattice, these values would coincide. Best agreement between the values is achieved in the homopolymer PVDF P100 sample. But, for all three samples, we can conclude that the lamellar stacks do not form ideal super-lattices.

From the self-correlation triangle, the linear fraction of phase 1, χ_1, is determined as $|A|/(|A|+Q)$ [36], and refers to the fraction characterized by the length, l_1. The values of χ_1 are included in Table 3. According to Babinet's principle [35], SAXS analysis does not allow unambiguous determination of the phase associated with l_1. In other words, phase 1 could refer either to the crystal or to the amorphous component. To

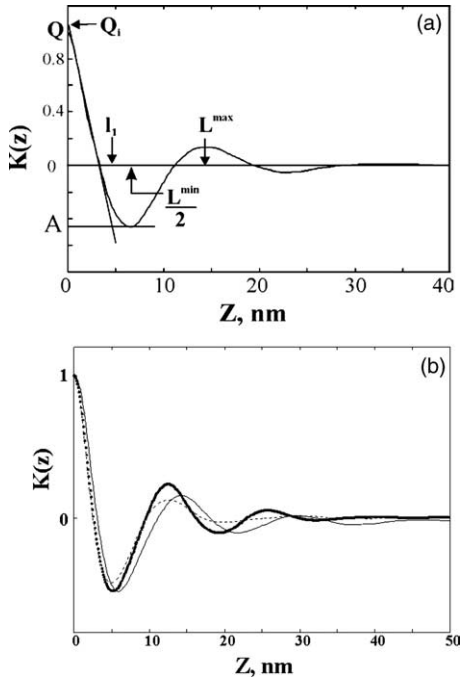

Fig. 11. One-dimensional electron density correlation function, $K(z)$ vs. z. (a) General correlation function, showing structural parameters characterizing the lamella stacks [36]; (b) PVDF/OMS nanocomposites; data taken at 140 °C. P100, PVDF homopolymer—filled circles; L0.01—solid line; L0.10—dotted line.

determine whether the crystal phase or the amorphous phase should be associated with length l_1, and linear fraction, χ_1, we perform the calculation of χ_L using Eq. (5) following the treatment of Santa Cruz [51]. We estimate the numerator of Eq. (5), converting mass fraction crystallinity into volume fraction using:

$$\chi_C^{vol} = \frac{\chi_C \rho_A}{[\rho_C - \chi_C(\rho_C - \rho_A)]} \quad (6)$$

where the PVDF amorphous and crystalline densities are $\rho_A = 1.667$ g/cm^3 [53], ρ_C(alpha) = 1.925 g/cm3 [6], and ρ_C(beta) = 1.973 g/cm3 [6]. Under the assumption that P100 and L0.01 are nearly all alpha phase, and L0.10 is nearly all beta phase, the volume fraction crystallinities from DSC are calculated, and are listed in Table 3.

The denominator, χ_L, of Eq. (5) can be either χ_1, or $(1-\chi_1)$, depending upon whether the shorter or the longer correlation length is associated with the crystals. If the longer length is selected, for example for P100, the calculation of χ_L will result in $\chi_L = 0.405/(1-0.295) = 0.57 > 1$, as required [51]. The linear stack crystallinity, χ_{CL}, and the fraction of material within the lamellar stacks, χ_L, are listed in Table 3. We conclude that for samples with small amounts of OMS, regardless of whether they contain predominantly alpha or beta crystallographic phase, the parameters describing the crystallinity of the stacks are about the same. Furthermore, as a result of the cold crystallization treatment used here, there is some amorphous material stranded outside of the lamellar stacks in PVDF/OMS nanocomposites.

Table 3
Thermal[a] and lamellar stack parameters[b] for slowly heated nanocomposites

Sample	P100	L0.01	L0.10
χ_c ($\pm$0.01)[c]	0.45	0.43	0.44
χ_C^{vol} ($\pm$0.01)[d]	0.405	0.40	0.40
L_B (nm) ($\pm$0.2)[e]	12.8	14.9	13.4
L^{max} (nm) ($\pm$0.2)[f]	12.5	14.0	12.7
L^{min} (nm) ($\pm$0.2)[g]	10.3	11.15	10.0
l_1 (nm) ($\pm$0.2)[h]	3.8	4.1	3.6
χ_1 ($\pm$0.01)[i]	0.295	0.29	0.27
χ_{CL} ($\pm$0.01)[j]	0.705	0.71	0.73
χ_L ($\pm$0.01)[k]	0.57	0.56	0.55

[a] Determined from DSC at heating rate of 1 °C/min.
[b] Determined at 140 °C from SAXS analysis.
[c] Mass fraction crystallinity from total area of the DSC endotherms using 104.6 J/g as heat of fusion of 100% crystalline PVDF [37].
[d] Calculated from Eq. (6).
[e] Bragg long period, L_B, from the maximum of Iq^2 vs. q.
[f] Long period, L_{max}, determined from the first maximum in $K(z)$ for $z>0$ [36].
[g] L_{min}, determined from twice the first minimum in $K(z)$ [36].
[h] Linear fraction of phase 1, l_1, determined from $K(z)$ using the self-correlation triangle [36].
[i] Volume fraction of phase 1, determined from $K(z)$ using $|A|/(|A|+Q)$ [36].
[j] Linear stack crystallinity, χ_{CL}, determined from $K(z)$ using the self-correlation triangle [36] and choosing the longer correlation length for the crystal thickness [51].
[k] Calculated from Eq. (5).

4. Conclusions

Nanocomposites of PVDF with Lucentite OMS have been investigated over a wide range of compositions, from 0.01 to 20% OMS by weight. The following summarizes the conclusions of this work on cold-crystallized samples:

1. Nanocomposites with OMS content above 0.5 wt% OMS show a Lucentite gallery spacing peak at a slightly higher d-spacing than observed in pure Lucentite OMS. This indicates there is some level of intercalation of PVDF within the OMS galleries.
2. For OMS greater than 0.5 wt%, alpha phase fraction, ϕ_{alpha}, is insignificant ($\phi_{alpha} \sim 0$–0.01).
3. No Lucentite gallery spacing peak is seen in samples with OMS content below 0.10 wt% OMS, suggesting that in these samples the OMS is exfoliated.
4. At the intermediate range, for OMS between 0.5 wt% down to 0.025 wt%, beta phase dominates and the beta fraction, ϕ_{beta}, is related to alpha by $\phi_{beta} > \phi_{alpha}$. The ability of such small amounts of OMS ($\sim$0.025 wt%) to cause beta crystal domination is remarkable.
5. At low OMS content, below 0.025 wt% OMS, alpha dominates and $\phi_{alpha} > \phi_{beta}$.

   Selected samples (P100, L0.01, and L0.10) were examined using real-time simultaneous wide and small angle X-ray scattering. These studies reveal that:
6. There is no inter-conversion between the alpha and beta phase PVDF crystals in L0.01 and L0.10 nanocomposites where these crystals coexist at room temperature.

7. The sample L0.10 containing predominantly beta phase has lamellar stacks that are not as well correlated as those in P100 or L0.01.

Future work [47] will report on real-time simultaneous wide and small angle X-ray scattering during melt crystallization to study the sequence of formation of alpha and beta phase PVDF crystals.

Acknowledgements

The authors thank the National Science Foundation, Polymers Program of the Division of Materials Research, for support of this research through grants DMR-0406127 and DMR-0100646. Undergraduate summer interns Buckley, Jenkins, Pan, and Washington performed the research reported herein, at Tufts University. A portion of the X-ray scattering work was conducted at the Brookhaven National Laboratory, National Synchrotron Light Source, Advanced Polymers Beamline X27C supported by the Department of Energy.

References

[1] Davies GR. In: Goodman C, editor. Physics of dielectric solids. Inst Phys Conf Series No. 58; 1980.
[2] Lovinger AJ. In: Basselt DC, editor. Developments in crystalline polymers-I. London: Applied Science Publishers; 1982.
[3] Kawai H. Jpn J Appl Phys 1969;8(7):1975.
[4] Lovinger AJ. Macromolecules 1981;14:322.
[5] Bachmann M, Lando J. Macromolecules 1981;14:40.
[6] Hasegawa R, Takahashi Y, Chatani Y, Tadokoro H. Polym J 1972;3:600.
[7] Matsushige K, Nagata K, Imada S, Takemura T. Polymer 1980;21:1391.
[8] Newman B, Scheinbeim J. Macromolecules 1983;16:60.
[9] Prest W, Luca D. J Appl Phys 1975;46:4136.
[10] Prest W, Luca D. J Appl Phys 1978;49(10):5042.
[11] Nandi A, Mandelkern L. J Polym Sci, Part B: Polym Phys 1991;29:1287.
[12] Tseng CR, Lee HY, Chang FC. J Polym Sci, Part B: Polym Phys 2001;39: 2097.
[13] Kim K, Ryu K, Kang SG, Chang S, Chung I. Macromol Chem Phys 2001; 202:866.
[14] Lincoln D, Vaia R, Wang Z, Hsiao B. Polymer 2001a;42:1621.
[15] Lincoln D, Vaia R, Wang Z, Hsiao B, Krishnamoorti R. Polymer 2001b;42:9975.
[16] Lincoln D, Vaia R, Krishnamoorti R. Macromolecules 2004;37:4554.
[17] Cho J, Paul D. Polymer 2001;42:1083.
[18] Fornes T, Paul D. Polymer 2003;44:3945.
[19] Wu Q, Liu X, Berglund L. Macromol Rapid Commun 2001;22:1438.
[20] Liu X, Wu Q. Eur Polym J 2002;38:1383.
[21] Nair S, Ramesh C. Macromolecules 2005;38:454.
[22] Priya L, Jog JP. J Polym Sci, Part B: Polym Phys 2002;40:1682.
[23] Priya L, Jog JP. J Polym Sci, Part B: Polym Phys 2003a;41:31.
[24] Priya L, Jog JP. J Appl Polym Sci 2003b;89:2036.
[25] Shah D, Maiti P, Gunn E, Schmidt D, Jiang D, Batt C, Giannelis E. Adv Mater 2004a;16(14):1173.
[26] Shah D, Maiti P, Jiang D, Batt C, Giannelis E. Adv Mater, doi 101002/adma200400984; 2004b.
[27] Buckley J, Cebe P, Cherdack D, Jenkins M, Pan J, Reveley M, et al. Am Chem Soc, Div Polym Mater: Sci Eng, Prepr 2005;93:753.
[28] Ramesh C, Gowd E. Macromolecules 2001;34:3308.
[29] Murthy N, Curran S, Aharoni S, Minor H. Macromolecules 1991;24:3215.
[30] Dennis HR, Hunter DL, Chang D, Kim S, White JL, Cho JW, Paul DR. Polymer 2001;42(23):9513.
[31] Mathias L, Davis R, Jarrett W. Macromolecules 1999;32:7958.
[32] Lee YH, Bur A, Roth S, Start P, Harris R. Polym Adv Technol 2005;16: 249.
[33] Pramoda KP, Mohamed A, Phang IY, Liu T. Polym Int 2005;54:226.
[34] Zen-Noh Unico America, Synthetic smectite data sheet formerly available at: http://www.unicoop.co.jp/en/products/main31.asp.
[35] Glatter O, Kratky O. Small angle X-ray scattering. London: Academic Press; 1982.
[36] Strobl G, Schneider M. J Polym Sci, Polym Phys 1980;18:1343–59.
[37] Nakagawa K, Ishida Y. J Polym Sci, Polym Phys 1973;11(11):2153.
[38] Cebe P, Runt J. Polymer 2004;45(6):1923.
[39] MATLAB™ The Mathworks. Natick, MA; 2000.
[40] Kobayashi M, Toshiro K, Tadokoro H. Macromolecules 1975;8(2):158.
[41] Tashiro K, Kobayashi M, Tadokoro H. Macromolecules 1981;14:1757.
[42] Bachmann M, Gordon W, Koenig J, Lando J. J Appl Phys 1979;50(10): 6106.
[43] Boccaccio T, Bottino A, Capannelli G, Piaggio P. J Membr Sci 2002;210: 15.
[44] Li J, Wang C, Zhong W, Zhang P, Wang Q, Webb J. Appl Phys Lett 2002; 81(12):2223.
[45] Lochhead RY, Boykin CM. In: Krishnamoorti R, Vaia RA, editors. Polymer nanocomposites: synthesis, characterization, and modeling. ACS symposium series 804. Washington, DC: American Chemical Society; 2002. p. 85–98.
[46] Crawford J, Cebe P. Unpublished DSC data; 2005.
[47] Alpern R, Amare D, Cebe P, Crawford J, Dolan B, Ince BS, Jones S, Kobylarz R, Reveley M. J Mater Sci. In preparation.
[48] Ogata N, Kawakage S, Ogihira T. Polymer 1997;38:5115.
[49] Maiti P, Nam PH, Okamoro M, Hasegawa N, Usuki A. Macromolecules 2002;35:2042.
[50] Jimenez G, Ogata N, Kawai H, Ogihara T. J Appl Polym Sci 1997;64: 2211.
[51] Santa Cruz C, Stribeck N, Zachmann HG, Balta Calleja F. Macromolecules 1991;24:5980.
[52] Vonk C, Kortleve G. Kolloid-Z 1967;19:220.
[53] Nakagawa K, Ishida Y. Kolloid ZZ Polym 1973;25:103.